Publications   **Bioengineering**

3-2011

In Vitro Validation of Finite Element Analysis of Blood Flow in Deformable Models

Ethan Kung

Andrea S. Les

C. Alberto Figueroa

Francisco Medina

Karina Arcaute

See next page for additional authors

Authors

Ethan Kung, Andrea S. Les, C. Alberto Figueroa, Francisco Medina, Karina Arcaute, Ryan B. Wicker, Michael V. McConnell, and Charles A. Taylor

5.1 Abstract

Purpose: To validate numerical simulations of flow and pressure incorporating deformable walls using *in-vitro* flow phantoms under physiological flow and pressure conditions.

Materials and Methods: We constructed two deformable flow phantoms mimicking a normal and a restricted thoracic aorta, and developed a physical Windkessel model to use as the outlet boundary condition. We then used magnetic resonance imaging, flow probes, and pressure catheters to acquire flow and pressure data in the phantom while it operated under physiological conditions. Next, *in-silico* numerical simulations were performed, and velocities, flows, and pressures in the *in-silico* simulations were compared to those measured in the *in-vitro* phantoms.

Results: The experimental measurements and simulated results of pressure and flow waveform shapes and magnitudes compared favorably at all of the different measurement locations in the two deformable phantoms. The average difference between measured and simulated flow and pressure was approximately 3.5 cc/s (13% of mean) and 1.5 mmHg (1.8% of mean), respectively. Velocity patterns also showed good qualitative agreement between experiment and simulation especially in regions with less complex flow patterns.

Conclusion: We demonstrated the capabilities of numerical simulations incorporating deformable walls to capture both the vessel wall motion and wave propagation by accurately predicting the changes in the flow and pressure waveforms at various locations down the length of the deformable flow phantoms.

5.2 Introduction

The stress and strain in blood vessels, as well as hemodynamic parameters such as the three-dimensional blood flow and pressure fields, have direct effects on the initiation and development of cardiovascular diseases such as atherosclerosis and aneurysms.[2,84,85] Knowledge of how *in-vivo* forces and tissue motions interact with implantable medical devices is also essential for understanding and predicting their behavior after implantation. For example, compliance mismatch between a prosthetic bypass graft and its adjacent native arteries has been hypothesized to lead to graft failure.[12] Medical imaging has been used to investigate vessel strain and blood flow hemodynamics, but with limited temporal and spatial resolutions, and often with discomfort to the patients as they are required to remain motionless for long periods during imaging sessions. Image-based computational fluid dynamics (CFD) methods, due to their minimal patient involvement and their ability to finely resolve time and space, have been a practical alternative to quantifying vessel strains and hemodynamic conditions for studies of disease mechanisms[15,17,18] and the design and evaluation of medical devices.[19-21] The ease of applying variations in geometry and flow conditions in the computational domain also motivates the use of CFD in the planning and prediction of surgical procedures.[22,23] Previous studies of cardiovascular CFD included the use of rigid wall models,[86] and dynamically deforming models.[87] Considering that vessel wall deformability often influences flow velocities and pressures, and that wave propagation phenomena can only be captured when considering wall deformation since blood behaves as an incompressible fluid, it is advantageous to include blood vessel deformability in numerical simulations whenever possible.

Much work remains to validate CFD methods against experimental data. Previous *in-vitro* validation studies have been performed only for the rigid case, likely due to the lack of realistic outflow boundary conditions, which are required to represent physical properties of downstream vasculature and to produce physiologic levels of pressure. For example, implementations of simple zero pressure boundary conditions in the physical setup where phantom outlets connect directly into a fluid reservoir[33,36,37]

would not be able to provide the pressures required to achieve realistic deformations in a compliant model.

In this study, we present results from two compliant phantoms under physiological flows and Windkessel boundary conditions for the validation of the numerical method incorporating wall deformability. The Windkessel boundary condition is a practical boundary condition prescription method in CFD simulations that can provide physiologically realistic impedances.[24,57,77] We built a normal and a restricted physical model (flow phantom) comparable in size to the descending thoracic aorta, and constructed a physical analog of the Windkessel model to be attached to the outlets of each flow phantom to provide physiologically-realistic outflow impedances. A 1.5T MRI system was then used to acquire phase-contrast magnetic resonance imaging (PCMRI) flow velocity data in multiple 2D planes in the phantoms while they were under pulsatile physiologically-realistic flow and pressure conditions. The use of PCMRI in this study enables us to follow a similar protocol for future *in-vivo* validation. Next, we performed *in-silico* numerical CFD simulations incorporating a coupled momentum method for wall deformability,[16] and prescribed Windkessel boundary conditions that directly corresponded to the physical setup. We then compared the flows, pressures, and velocity patterns measured in the *in-vitro* phantoms to those computed in the *in-silico* CFD simulations.

5.3   Methods

5.3.1   Physical Flow Phantom Construction & Characterization

We constructed two flow phantoms each containing a compliant vessel with an unpressurized diameter of 2cm, length of 25 cm, and thickness of 0.08 cm. The diameters and thicknesses of the vessels were selected such that physiological diameters[88,89] and strains[90,91] mimicking the descending thoracic aorta would be achieved under physiological operating pressures. One of the vessels was constructed to be a simple straight cylinder, and the other to be a straight cylinder containing a stenosis of diameter 0.88 cm at its center, which equivalents to an 84% area reduction relative to the mean operating diameter of the phantom.

To fabricate a compliant vessel, we used a multi-step dip-spin coating technique which entailed dipping an aluminum rod machined to the desired inner geometry of the vessel into a silicone mixture.[92,93] The important factors in obtaining the desired vessel wall thickness were the silicone mixture viscosity, dipping withdrawal speed, rod diameter, and number of dips. We set the silicone viscosity to 1500-2000 cp, dipped the aluminum rod vertically into the silicone mixture, and withdrew it at a controlled speed of 23.8 centimeters per minute. To obtain a uniform thickness circumferentially, we then set the rod on a horizontal rotating fixture for 30 minutes while the silicone dried. The entire process was repeated twice to obtain the desired thickness of 0.08 cm. Finally, the rod was set to cure in a heat convection oven at 100 °C for 4 hours.

We connected the inlet and outlet of each compliant vessel to a rigid section of flow conduit in order to allow for easy connection to the rest of the experimental flow setup. We also glued the bottom edge of the vessel along a ridge of width 6.8mm using a small amount of epoxy (5 Minute Epoxy, Devcon, MA) to mimic the *in-vivo* tethering of arteries to surrounding tissues such as the spine. The rigid inlet and outlet sections, together with the compliant vessel glued to the ridge, made up a "flow phantom." For the stenotic phantom, a rigid ring was placed around the stenosis to make this region of the compliant vessel essentially "rigid". This mimics the *in-vivo* material property of an arterial stenosis comprised of a stiff plaque.

We performed static pressurization tests to characterize the phantom deformation under different levels of pressures. We pressurized the phantoms using a syringe while monitoring the internal pressure with a catheter pressure transducer ("Mikro-Tip" SPC-350, Millar Instruments, Houston, TX). The outer diameter of the compliant vessels at various pressurization levels was measured using a digital caliper (CD-6" CS, Mitutoyo Corp., Kawasaki, Japan). Figure 5.1 shows the static pressurization characterization data for the two phantoms. There was an approximately linear relationship between the expansion of the compliant vessels and the increasing static pressures within the expected operating pressure range.
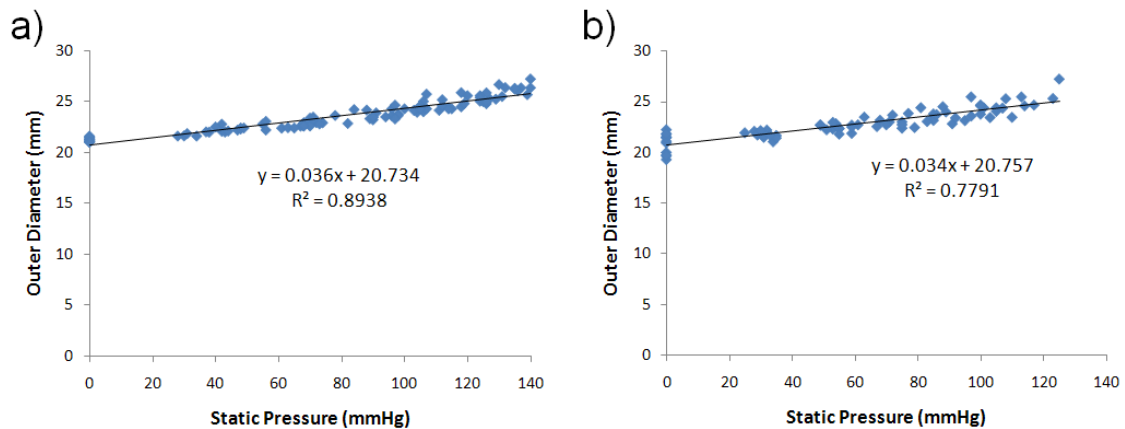
Figure 5.1 Vessel Outer Diameter Versus Static Pressure for the a) Straight Phantom, and b) Stenotic Phantom

We also characterized the viscoelastic properties of the silicone material using a dynamic mechanical analyzer (DMA Q-800, TA Instruments, New Castle, DE). We took small rectangular pieces (20 x 5 x 0.7mm) of the silicone material, and tested them using a multi-frequency sweep controlled strain method. We applied a pre-load of 0.45N in order to deform the material to an approximately 12% static strain, we then applied an oscillating strain of 5% over a range of incremental frequencies from $0.10 - 6.0$ Hz. These settings approximately correspond to the operating conditions of the phantoms in the flow experiments. When subjected to an oscillating strain at 1Hz, the storage moduli (which represent the elastic behavior of the material) in all of the six different samples tested were approximately 10% higher compared to when subjected to an oscillating strain at 0.1Hz.

5.3.2 **Outlet Boundary Condition**

We used a four-element Windkessel model consisting of an inductance (L), proximal resistance (R_p), capacitance (C), and distal resistance (R_d), at the outlet boundary of the phantom (Figure 5.2). Physically, the Windkessel module was designed such that physiologically realistic flows and pressures were achieved in the phantom, and

that the specific values of the resistance and capacitance components remained reasonably constant over the operating range of each experiment.

We constructed the resistance module by placing a large number of thin-walled glass capillary tubes (Sutter Instrument, CA) in parallel with each other inside a plexiglass cylinder. Using Poiseuille's law and the equation for parallel resistances, the resistance value of the module is:[69] Resistance=8 μ l/(Nπr4), where μ is the dynamic viscosity of the working fluid, l is the length of the capillary tubes, N is the total number of capillary tubes in parallel, and r is the inner radius of each individual capillary tube. We used 129 capillary tubes with inner diameters of 0.156 cm, and 125 tubes with inner diameters of 0.078 cm, for R_p and R_d, respectively. The theoretical resistance values corresponding to the specific viscosity of the working fluid in each of the two phantom experiments are listed in Table 5.1.

The capacitance of a fluid system is C=ΔV/ΔP where ΔV and ΔP are the changes in volume and pressure. In a closed system at constant temperature, an ideal gas exhibits the behavior PV=(P+ΔP)(V-ΔV), where P and V are the reference pressure and volume. The capacitance of a pocket of air is then: C = (V - ΔV) / P. For small changes in volume relative to the reference volume, a reasonably constant capacitance can be obtained with an air pocket. We constructed the capacitance module with a plexiglass box that can trap a precise amount of air to act as a capacitance in the system. The capacitance box has an inlet and an outlet, and as the fluid enters and exits the box, the fluid level in the box rises and falls slightly. The varying fluid level contributes to an additional capacitance that is in series with the capacitance due to air compression. This additional capacitance, if significantly larger than the air compression capacitance, has minimal impact on the overall capacitance. The capacitance due to the varying fluid level is proportional to the cross-sectional area of the box. In the actual construction of the capacitance module, we made the box sufficiently large such that the capacitance contribution from the varying fluid level can be disregarded. We also designed a smooth contour for the inlet of the module in order to minimize flow turbulence and thus avoid parasitic resistances. The air volume we used in the capacitor module was 210mL and 300mL at ground pressure (atmosphere pressure), for the straight and stenotic phantom

experiment, respectively. The theoretical capacitance at the average operating pressure (relative to ground) of 100mmHg and 91mmHg for the straight and stenotic phantom experiments, respectively, is listed in Table 5.1.

The flow inductance results from the fluid momentum, and can be calculated from the geometry of the physical system. The flow inductance in a fluid conduit is: $L = \rho l/A$, where l and A are the length and the cross-sectional area of the conduit, respectively. The theoretical inductance of the Windkessel module used in the phantom experiments is listed in Table 5.1.

	Straight Phantom Experiment		Stenotic Phantom Experiment	
	Theoretical	Experimental	Theoretical	Experimental
L (Barye s^2 cm^{-3})	7	7	7	7
Rp (Barye s cm^{-3})	246	242	241	259
C (cm^3 Barye^{-1})	1.6 e^{-4}	1.3 e^{-4}	2.3 e^{-4}	1.9 e^{-4}
Rd (Barye s cm^{-3})	4055	3990	3980	4279

Table 5.1 Theoretical and Experimental Windkessel Component Values for the Straight and Stenotic Phantom Experiments
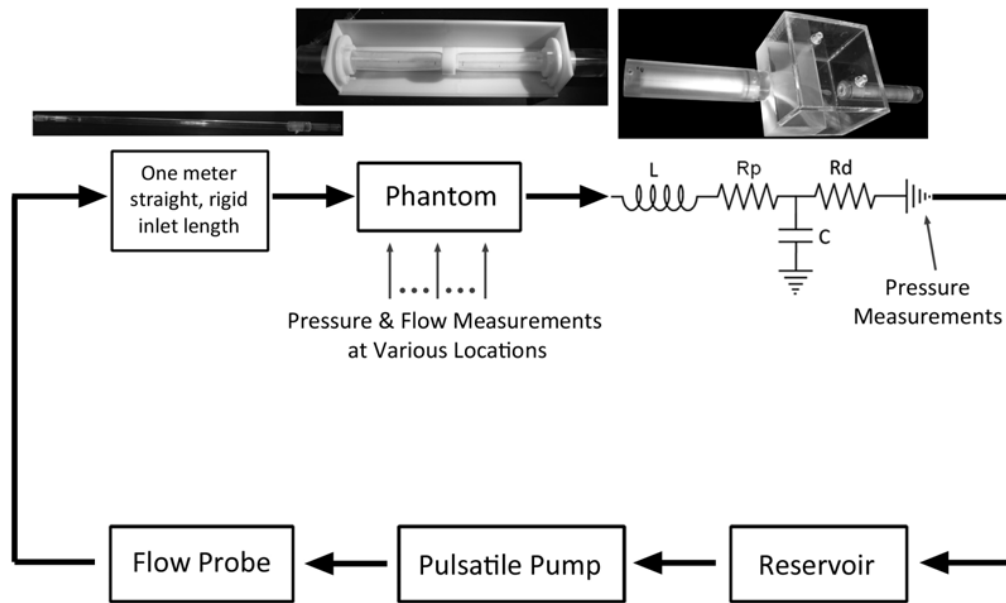
5.3.3　In-vitro Experiment

Figure 5.2 *In-vitro* Flow Experiment Setup Diagram

We performed two *in-vitro* experiments, one with each flow phantom. For each experiment, the flow phantom and the outlet impedance module were placed in a flow system as shown in Figure 5.2. To produce the input flow to the phantom, we used a custom-built, MR-compatible, computer-controlled pulsatile pump to physically reproduce flow waveforms similar to the descending aortic flow measured in patients with aortic coarctations.[94] Immediately upstream of the phantom we placed one meter of straight, rigid tubing, a honeycomb flow straightener, and two pressure-stabilization grids, in order to provide sufficient entrance conditioning to generate a stable and fully-developed Womersley flow profile at the phantom inlet. The working fluid in the flow system was a 40% glycerol solution with a dynamic viscosity similar to that of blood, and contained 0.5% Gadolinium. The fluid viscosity for the straight and stenotic phantom experiments was measured to be 0.0461 poise and 0.0452 poise, respectively.

We inserted MR-compatible catheter pressure transducers ("Mikro-Tip" SPC-350, Millar Instruments, Houston, TX) through small ports on the sides of the phantom to

capture pressure waveforms at various locations within the phantom (Figure 5.3), and also immediately downstream of the outlet impedance module.   The signals from each catheter pressure transducer were sent into a pressure control unit (TCB-600, Millar Instruments, TX) which generates an electrical output of 0.5V per 100mmHg of pressure. An MR-compatible ultrasonic transit-time flow sensor was used to monitor the total input flow to the phantom. We placed the externally clamped flow probe (8PXL, Transonic Systems, NY) around a short section of Tygon tubing R3603 immediately upstream of the one-meter flow conditioning rigid tubing, and sent the signals from the probe into a flowmeter (TS410, Transonic Systems, NY) with its low pass filter setting at 160Hz. The data from the flow meter and the pressure control units was recorded at a sample rate of 96 samples per second using a data acquisition unit (USB-6259, National Instruments, Austin, TX) and a LabVIEW program (LabVIEW v.8, National Instruments, Austin, TX). For each data acquisition, we averaged approximately 50 cycles of flow and pressure data to obtain one representative cycle of flow and pressure waveforms. The flow and pressure waveforms were stable in between the cycles of each acquisition. We used the pressures measured downstream of the outlet impedance module as the ground reference, and subtracted it from all of the other pressure measurements to obtain the true pressure waveforms relative to the ground pressure.

We acquired through-plane flow velocity data at different locations within the phantoms (Figure 5.3) using a cardiac-gated 2D cine PCMRI sequence in a 1.5T GE MR scanner (Signa, GE Medical Systems, Waukesha, WI) and an 8-channel cardiac coil. The imaging parameters were: 256x192 acquisition matrix reconstructed to 256x256, 18×18 cm^2 field of view, 5mm slice thickness, TR=11~14 ms, TE=5~7 ms, 20 degree flip angle, and NEX=2. A velocity encoding gradient of 50 cm/s was used for all measurements, except for the L2, L3, and L4 measurements of the stenotic phantom, where the velocity encoding gradient was 100, 200, and 100 cm/s, respectively. The LabVIEW program which controlled the pulsatile pump produced a trigger signal that was converted by an electrocardiogram (ECG) simulator (Shelley Medical Imaging Technologies, London, Ontario, Canada) into an ECG signal used by the MRI system for gating, and 24 time points per cardiac cycle synchronized to this ECG signal were

reconstructed. The temporal resolution of the velocity data was double the TR (~26ms). We placed vitamin E capsules (Schiff Nutrition Group, Inc, Salt Lake City, UT) as well as saline bags around the flow region of each acquisition location to produce the reference signals of stationary fluids, which were then used for baseline eddy current correction with a linear correction algorithm in the analysis of the PCMRI data.
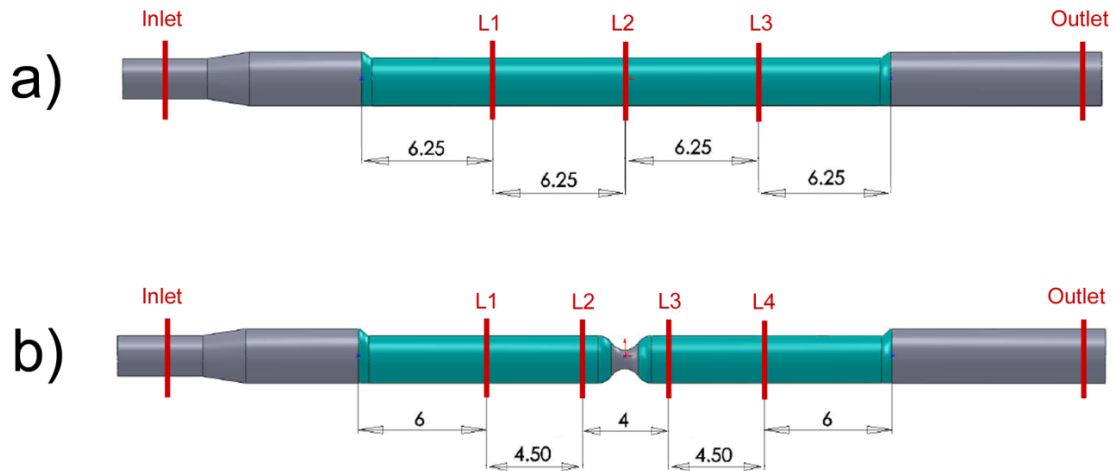

Figure 5.3 Pressure and Flow Velocity Measurement Locations in a) the Straight Phantom, and b) the Stenotic Phantom. Green section is deformable. Grey section is rigid. Dimensions are in centimeters

5.3.4   In-silico Simulation

We performed the numerical simulation of blood flow and pressure using a custom stabilized finite-element method to solve the incompressible Navier-Stokes equations.[95] The deformability of the wall is incorporated by a coupled momentum method developed by Figueroa et al., which adopts a linearized kinematics formulation for the solid domain, and allows for a fixed fluid mesh and nonzero fluid velocities at the fluid-solid interface[16]. The end result is that the effects of wall motion are embedded into the fluid equations simply as additional terms defined on the fluid-solid interface, leading to minimal increases in implementation complexity and computational efforts compared to rigid wall formulations.

Due to the fixed fluid mesh and linearized wall mechanics implementation of the coupled momentum method, we must use a mesh that most closely resembles the average geometry of the phantom during its operation. Calculations of the solid domain behavior require the definition of the elastic modulus of the vessel wall material. The data from the static tests of the compliant phantoms shown in Figure 5.1 can be used to find the radii of the compliant tubes at their respective average operating pressures, and the elastic modulus of the silicone material.

An analytical equation describing the expansion of a pressurized circular, cylindrical vessel made of an isotropic material and under small strain is:[96]

$$E = 1.5 \frac{\Delta P R_i^2 R_o}{\left(R_o^2 - R_i^2\right) \Delta R} \tag{5.1}$$

where E is the elastic modulus of the material, R_i is the reference inner radius of the vessel, R_o is the reference outer radius of the vessel, ΔP is the change in pressure, and ΔR is the resulting change in radius.

Equation 5.1 describes a linear relationship between ΔR and ΔP. R_o is related to R_i by the vessel wall thickness, which we assume remains unchanged over small strains. Using the experimentally measured average operating pressure in the phantom, and prescribing the values of E and R_i, a plot of theoretical diameter versus pressure graph similar to Figure 5.1 can be generated. For each phantom, we modify the values of E and R_i until the theoretical plot coincides with the linear best fit of the static pressurization test results shown in Figure 5.1, and determine the operating radius of the phantom, as well as the elastic modulus of the silicone material. The operating radius was determined to be 1.13 cm at the operating pressure of 96 mmHg for the straight phantom, and 1.11 cm at the operating pressure of 89 mmHg for the stenotic phantom. The static elastic modulus of both phantoms was $9.1\text{x}10^5$ Pa. Using the result of the dynamic mechanical analysis previously discussed in the phantom characterization section, the effective elastic modulus of the silicone material at the fundamental operating frequency of the experiments (1 Hz) was then $1.0\text{x}10^6$ Pa.

At the outlet boundary, we prescribed a Windkessel model (Figure 5.4) with the lumped-parameter component values determined from the experimentally measured flow

and pressure at the phantom outlet. Mass conservation dictates that the average flow throughout different locations in the phantom is constant. For the analysis of Windkessel component values, we offset the outlet PCMRI flow measurement such that the average flow is equal to that measured by the flow probe, in order to exclude any effects of background correction variations. We used the measured average flow and pressure values at the phantom outlet to determine the total Windkessel resistance (R_p+R_d). The experimentally determined total Windkessel resistance in the straight and stenotic phantom experiment was 1.6% lower, and 7% higher, respectively, compared to theoretical. We used this ratio to scale the theoretical R_p and R_d to obtain the experimental values of the resistances. We then performed an analysis of the Windkessel model impedance:

$$Z(\omega) = j\omega L + R_p + \frac{R_d}{1+j\omega C R_d} \qquad (5.2)$$

to determine the value of the capacitance that will result in an impedance best reflecting the measured pressure and flow relationship at the phantom outlet. We prescribed these experimentally determined Windkessel component values (as listed in Table 5.1) in the numerical simulations. For the stenotic phantom simulation, due to the presence of turbulence in the domain, an augmented lagrangian method was used at the outlet to constrain the shapes of velocity profiles to prevent divergence.[97] This technique has been shown to have very little effect to the flow and pressure calculations in the numerical domain.[97]

We constructed computational 3D solid models from the physical construction details and the operating radii of each phantom. Each 3D solid model was discretized into an isotropic finite-element mesh with a maximum edge size of 0.1 cm using commercial mesh generation software (MeshSim, Simmetrix, Inc., NY). For the stenotic phantom mesh, we further refined a region of length 8cm distal to the stenosis using a maximum edge size of 0.03 cm, followed by another region of 4 cm downstream discretized using a maximum edge size of 0.06 cm. The straight phantom and stenotic phantom mesh contain approximately 1.5 million, and 3.5 million linear tetrahedral elements, respectively. Sections of the vessel wall boundary in the meshes were set to be

rigid or deformable according to the physical construction of each phantom (Figure 5.4). We set the initial values of pressure and vessel wall distention in the mesh based on the average pressure in the physical experiment and the vessel wall properties. We then mapped the flow waveform measured by the flow probe to the inlet face of the computational domain using a Womersley velocity profile (Figure 5.4). In the simulations we used a time step size of 0.42 milliseconds which resulted in 2400 time steps per cardiac cycle. For the straight phantom simulation, we simulated 5 cardiac cycles and used the data from the last cycle where the pressures had stabilized in the final analysis. For the stenotic phantom, due to the presence of cycle-to-cycle variations in the velocity pattern, we simulated 14 cardiac cycles and used the ensemble-averaged data from the last 10 cycles in the final analysis. Since the PCMRI technique combines measurements acquired over multiple cycles into one cycle of velocity data, we ensemble-averaged the stenotic phantom simulation results to mimic the PCMRI data acquisition method.[37]
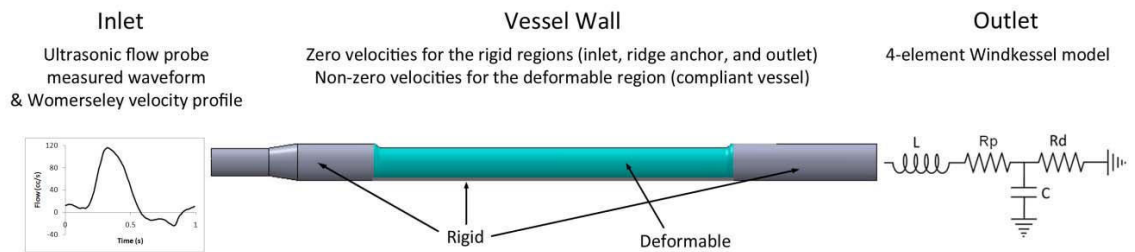

Figure 5.4 Summary of Boundary Condition Prescriptions for the Numerical Simulations

5.4   Results

5.4.1   Flow & Pressure Waveforms in the Straight Phantom

Figure 5.5 compares the *in-silico* and *in-vitro* flow and pressure waveforms and normalized pulse amplitudes at various locations in the straight phantom. There is good agreement between the simulated and measured waveform shapes and amplitudes for both flow and pressure, throughout the various locations in the phantom. The average difference between the measured and simulated flows is 3.7 cc/s, which is 12% of the average flow (31 cc/s). The average difference between the measured and simulated pressures is 2.0 mmHg, which is 2.4% of the average pressure (85 mmHg). In both the simulation results and experimental measurements, we clearly observe progressive flow waveform damping, as well as progressive pressure waveform pulse amplitude increase, down the 25cm length of the deformable vessel. A significant pressure waveform shape change occurs between the inlet and L1, which is the transition from the rigid section into the deformable section. The most prominent pressure pulse amplitude increase also occurs between the inlet and L1. The experimental measurements show that, of the approximate 10% increase in the normalized pressure pulse amplitude from the inlet to the outlet, roughly 7% occurred at the inlet and L1 transition. Lastly, both simulation and measurement showed an approximately 50% decrease in the normalized flow pulse amplitude between the inlet and the outlet of the phantom.
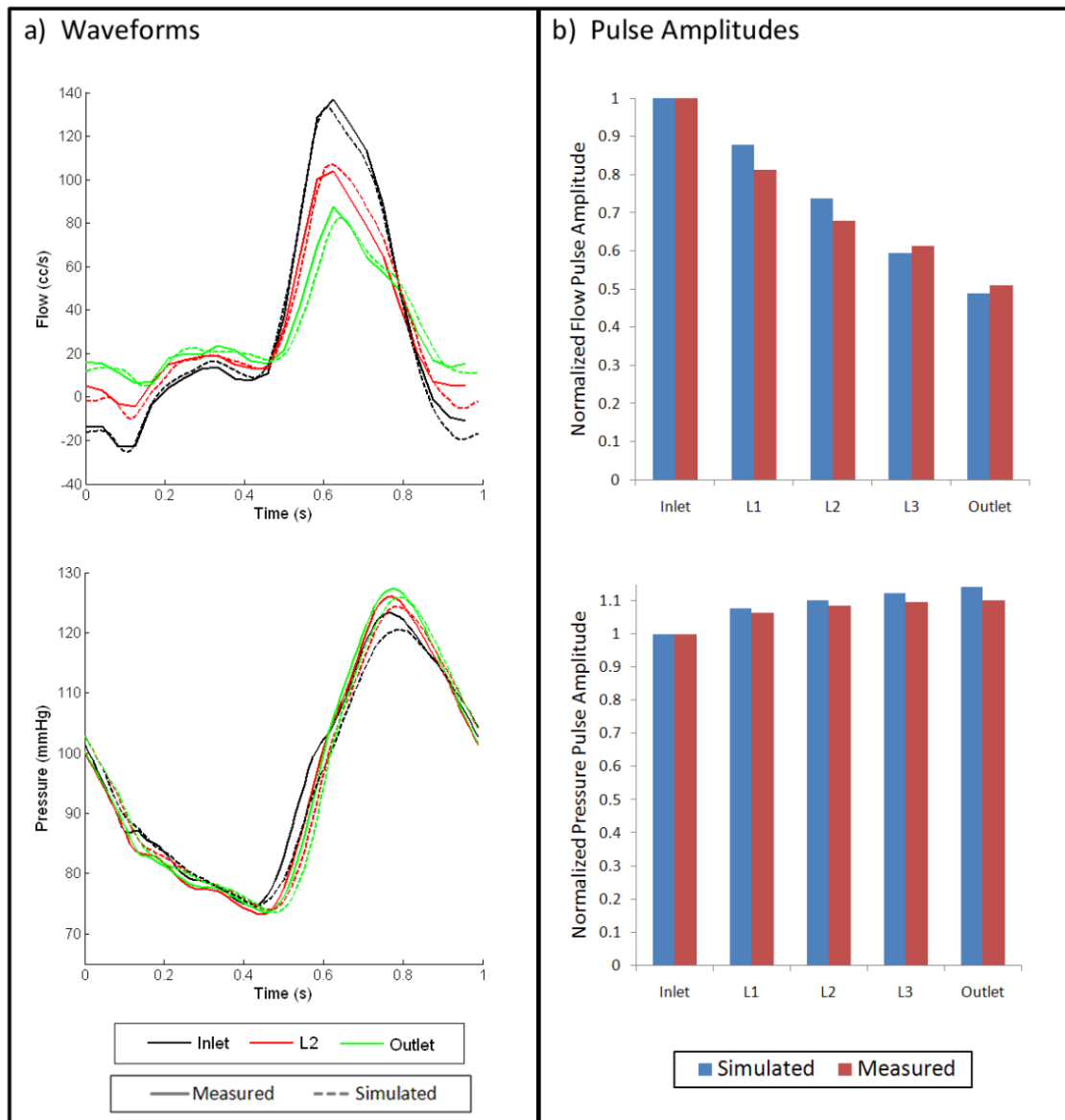
Figure 5.5 Straight Phantom Simulated Versus Measured Flow & Pressure a) Waveforms and b) Normalized Pulse Amplitudes, at Different Locations

5.4.2   **Flow & Pressure Waveforms in the Stenotic Phantom**

Figure 5.6 shows the comparisons of flow and pressure waveforms and normalized pulse amplitudes at various locations in the stenotic phantom.   The average difference between the measured and simulated flow waveforms is 3.4 cc/s, which is 13% of the average flow (26 cc/s). The average difference between the measured and simulated pressure waveforms is 1.0 mmHg, which is 1.2% of the average pressure (82 mmHg). We observe similar trends in pressure and flow behavior down the length of the stenotic phantom as those seen in the straight phantom. Between L2 and L3 of the stenotic phantom (across the stenosis), there is no visible difference in the flow waveforms, but there is a significant pressure drop. The drop in the peak pressure across the stenosis is 3.8 mmHg in the simulation, and 4.8 mmHg in the experimental measurement. The decrease in the normalized pressure pulse amplitude across the stenosis is 8.1% and 11.6% in simulation and measurement, respectively. A significant pressure waveform shape change occurred across the stenosis and is reflected in both measurement and simulation. As in the straight phantom case, the most prominent pressure pulse amplitude increase also occurs between the inlet and L1, which is the transition from the rigid section into the deformable section. The experimental measurements show that, of the 7% increase in pressure pulse amplitude between inlet and L2, about 6% occurred between the inlet and L1 transition. Both simulation and measurement show only an approximately 40% (compared to 50% in the straight phantom) decrease in the flow pulse amplitude between the inlet and the outlet of the stenotic phantom.
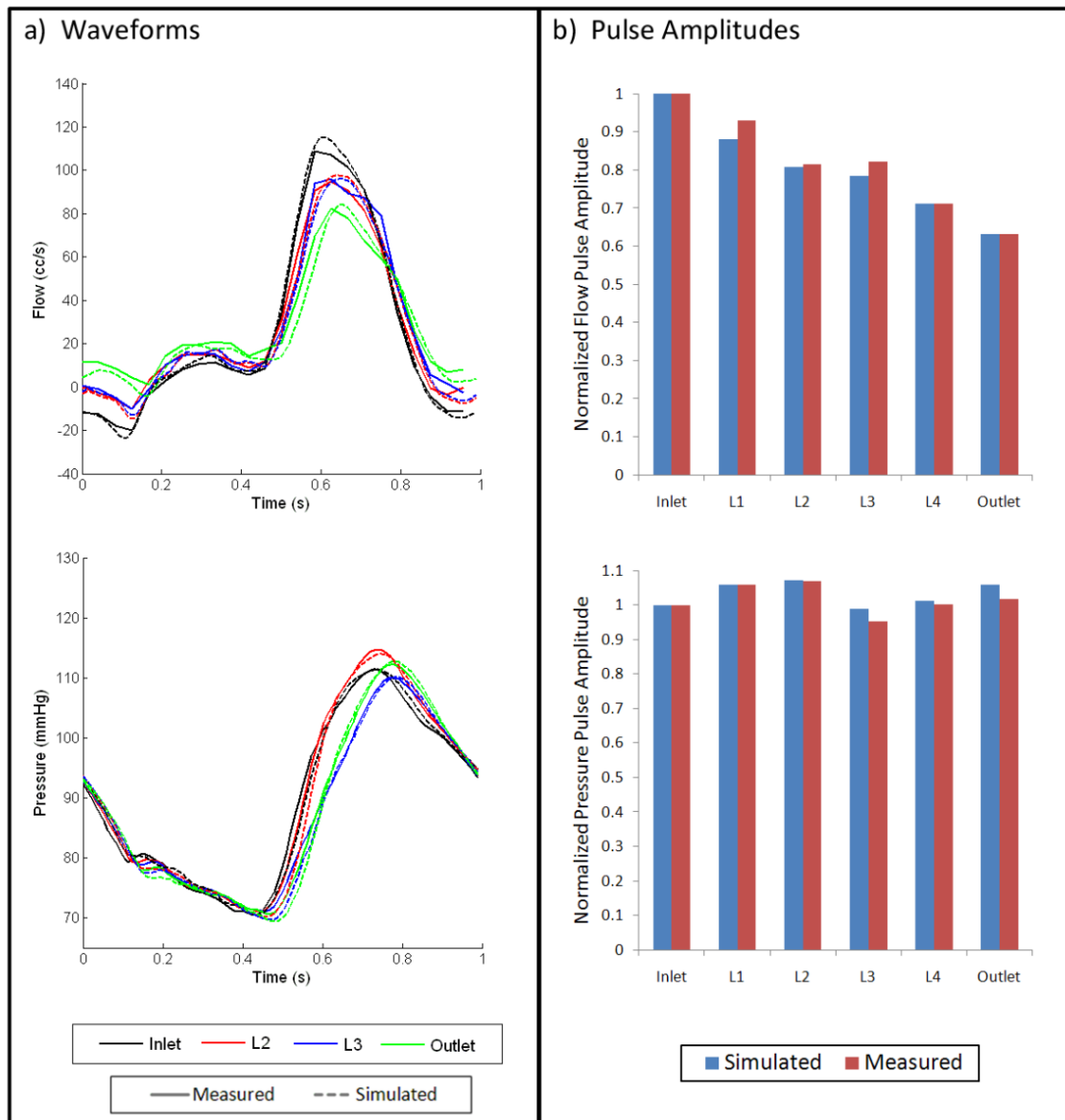
Figure 5.6 Stenotic Phantom Simulated Versus Measured Flow & Pressure a) Waveforms and b) Normalized Pulse Amplitudes, at Different Locations

5.4.3 Impedance Modulus & Phase at the Inlet / Outlet

We compare the impedance modulus and phase at the phantom inlet and outlet between simulation and measurement in Figure 5.7. In both phantom experiments, there is agreement between the simulated and measured impedance across physiologically

relevant frequencies. For the impedance phase, the experimental measurements exhibited more fluctuations at the higher frequency range compared to the simulated results. For frequencies in the 1~3 Hz range, both the simulation and measurement show that the impedance modulus increases from the inlet to the outlet. For both phantoms, the general shapes and magnitudes of the impedance modulus and phase compare favorably with those measured *in-vivo* in previous studies.[61,64,69]
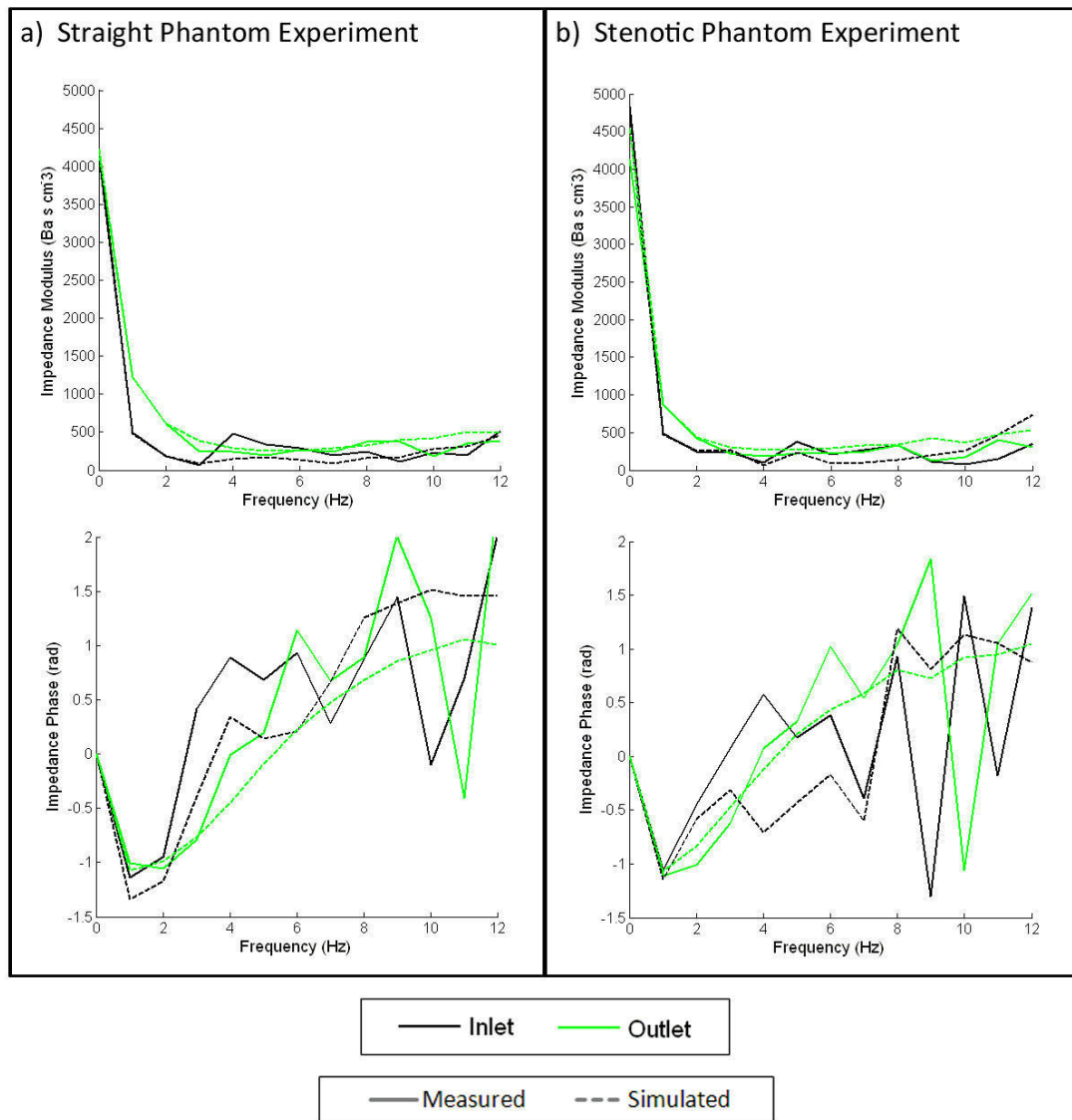

Figure 5.7 Simulated Versus Measured Impedance Modulus and Phase at the Inlet and Outlet for the a) Straight, and b) Stenotic Phantom Experiment

5.4.4   **Through-Plane Velocity Patterns**

We compare the simulated and measured through-plane velocity patterns at four different time points in the cardiac cycle: diastole, acceleration, peak systole, and deceleration. Figure 5.8 shows results for the L2 location in the straight phantom experiment. There is excellent qualitative agreement between the simulated and measured velocity pattern at all four time points. At acceleration and systole, there is forward flow of similar magnitudes and shapes across the slice, and a visible layer of decreased flow velocities near the vessel wall in both simulation and experiment. At diastole and deceleration, both simulation and experiment showed forward flow near the center, and a prominent region of backflow at the perimeter of the vessel. We generally observed a sustained Womersley velocity profile throughout the different locations in the straight phantom. Figure 5.9 shows flow velocity comparison results for the L2 and L3 locations in the stenotic phantom. In the L2 location, the pre-stenosis location in the stenotic phantom, we found nearly identical results as those presented for the straight phantom. In L3, the post-stenosis location, both simulation and measurement show a circularly-shaped jet of high forward velocities near the vessel center, and backward velocities (recirculation) around the vessel perimeter at the systole and deceleration time points. While the high velocity jet in the simulation contains slight irregularities in its shape, its size is comparable to that in the measured results.
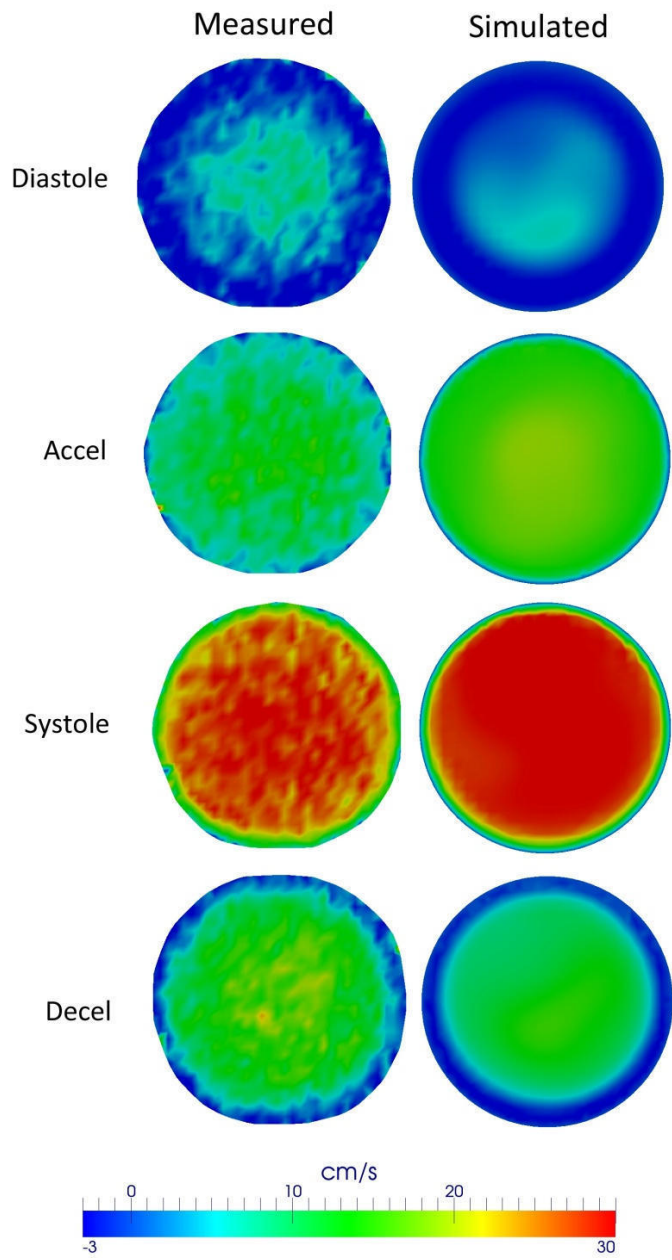
Figure 5.8 Through-Plane Velocity Pattern Comparisons at the L2 Location for the Straight Phantom Experiment at Four Different Time Points: Diastole, Acceleration, Systole, and Deceleration
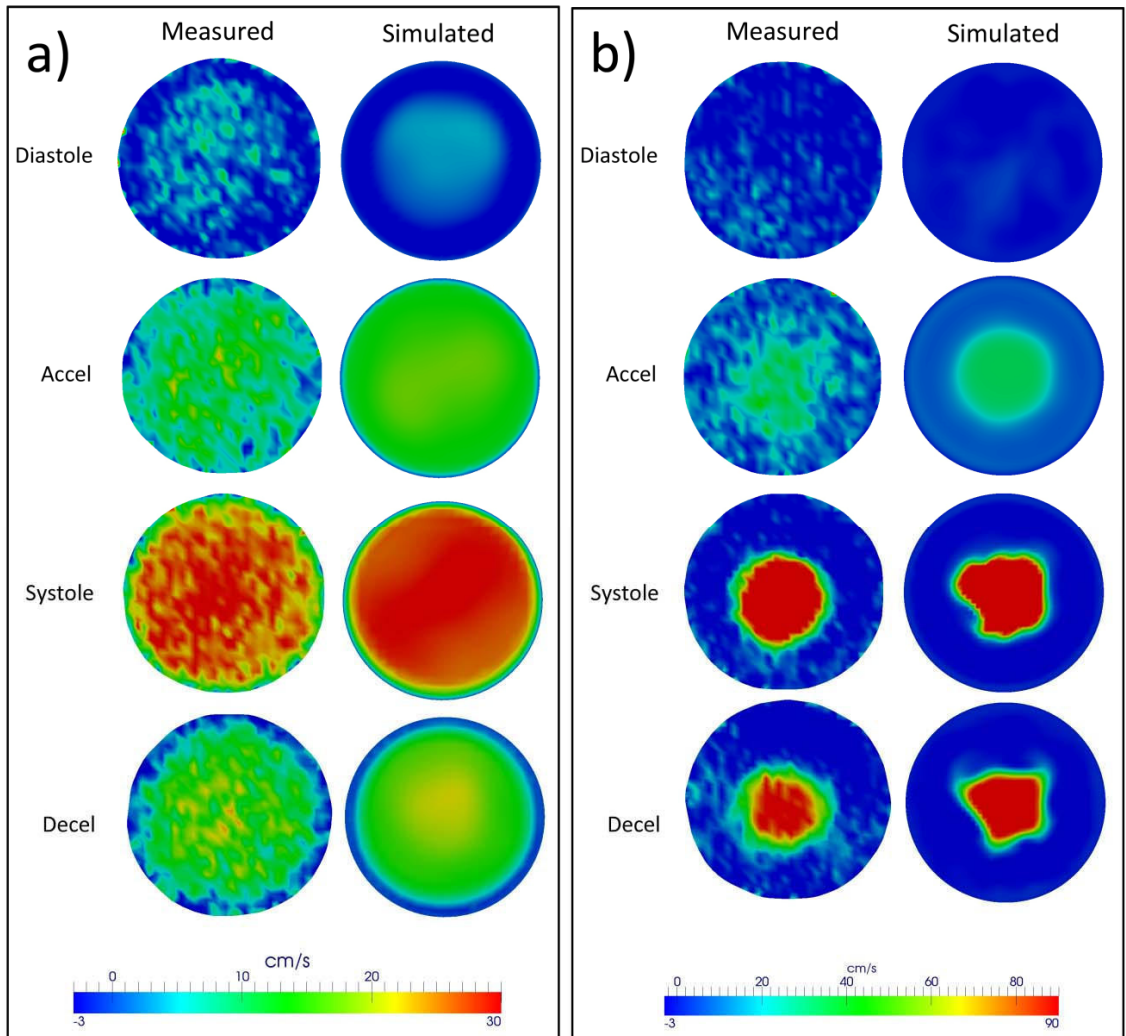
Figure 5.9 Through-Plane Velocity Pattern Comparisons at the a) L2, and b) L3 Location for the Stenotic Phantom Experiment at Four Different Time Points: Diastole, Acceleration, Systole, and Deceleration

5.5 Discussion

Figures 5.5 and 5.6 show that physiological flows and pressures[94,98] were achieved in the experiments. The damping of the flow waveform down the length of the phantom is the result of the flow being temporarily stored in the deformable tube, which essentially acts as a capacitance in the system. Since there is a rigid section at the center of the stenotic phantom, the total amount of deformable section is smaller compared to

that in the straight phantom. With less deformable volume to absorb the flow pulse, the inlet waveform is better preserved and we indeed observed smaller flow waveform damping between the inlet and outlet in the stenotic phantom. The accurate numerical prediction of flow waveform shapes and magnitudes at different locations down the length of the phantoms indicates that the calculated fluid velocities at the vessel wall boundary accurately correspond to the physical vessel wall movement, faithfully capturing the compliant behavior of the vessel. The prediction of the decrease in the flow waveform peaks down the length of the phantom requires accurate calculations of the vessel wall expansion in response to the increase in pressure, where additional fluid is stored in the vessel during the systolic period. On the other hand, the prediction of the gradual increase in flow waveform minimums requires accurate calculations of the elastic behavior of the vessel wall, which releases the stored fluid during the diastolic period. The flow waveform damping behavior observed in the simulations and experiments is generally consistent with the actual blood flow behavior *in-vivo*, where the pulsatility resulting from the pumping heart is damped out throughout the vasculature, and eventually transformed into steady flow in the capillaries.

Since a significant portion of the cardiac cycle was diastole where the flow was low or retrograde, the average flow rates were relatively low compared to systolic flow rates. The average difference of approximately 3.6 cc/s between the measured and simulated flow was 12~13% relative to the average flow rates, but was only under 5% relative to the systolic flow rates, which were between 80~140 cc/s.

The progressive increase of pressure pulse amplitude down the length of the phantom is also consistent with the *in-vivo* observation where the pulse pressure progressively increases from the brachial artery downstream towards the radial artery.[99] It has been generally believed that such phenomenon is attributed to the increased stiffness of the downstream arteries. Our experimental and simulation results suggest that wave propagation and reflection alone could contribute to a pressure pulse increase under the condition of constant vessel stiffness.

Across the rigid and deformable junction where there is a mismatch in characteristic impedances, the change in the pressure waveform shape and the prominent

increase in the pressure pulse amplitude could be attributed to wave reflections. Across a stenosis, pressure waveform changes also occur due to energy losses in the post-stenosis turbulent flow region. The numerical simulation accurately captured both the wave reflections between the rigid and deformable sections, and the energy loss across a stenosis, accurately predicting the changes in the pressure waveform at different locations within the straight and stenotic phantoms.

The impedance modulus increase between the phantom inlet and outlet during the 1-3Hz frequency range reflects the capacitive effect of the deformable tube. Pulsatile flow enters the inlet with relative ease due to the compliance in the deformable vessel downstream, resulting in a lower impedance modulus. At the outlet of the phantom, there is no deformable region downstream to manifest the effect of the lowered resistance to pulsatile flow. This phenomenon is only prominent in the lower frequency range partly because of the physical characteristics of the deformable tube dictating its response to dynamic strain, and partly because of the low modulus values in the higher frequency region making any differences difficult to observe. The increased prominence of outlet impedance phase oscillations at the higher frequency region in the experimental measurements could be due to the small high frequency component in the flow and pressure waveforms, making the noise in the measurements relatively high.

The favorable comparison in velocity patterns between simulation and measurement for the straight phantom is consistent with our expectation due to the trivial geometry of the phantom. We also expect the pre-stenosis location in the stenotic phantom to show similar results since complex flow originates from the stenosis and propagates to the regions downstream. At the L3 location in the stenotic phantom, which is immediately downstream of the stenosis where complex and recirculating flow occurs, the simulation showed a smooth contour for the flow pattern right up to the time frame immediately prior to peak systole. After which point the flow begins to decelerate and diverge, resulting in slight irregularities in the shapes of the flow patterns in the simulation results. We found that the irregularities in the flow pattern shapes were correlated with mesh resolution, where a simulation computed on a finer mesh resulted in fewer irregularities. In regions containing complex and diverging flow, it is thus

important to define a desired balance between flow pattern prediction accuracy and computational cost.

The vessel wall motion in the numerical simulation is sensitive to the prescribed thickness and elastic modulus of the vessel wall. Both the wall motion and the prescribed vessel geometry affect the volumetric flow and the pressure changes down the length of the vessel. Prescription of higher elastic modulus or smaller vessel diameter would result in diminished wall motion and smaller flow waveform damping, and vice versa. The method we developed to determine the relevant geometry and vessel wall properties requires direct manipulations and observations of the vessel which are only possible *in-vitro*. To apply the numerical simulation in an *in-vivo* setting, additional methods would need to be developed to determine the equivalent values of vessel parameters for the numerical model.

In conclusion, in this study we have produced a set of in-vitro, high-quality experimental data that can be used to compare against CFD results of flow and pressure within a compliant vessel under physiological conditions. The deformable CFD simulation utilizing the coupled momentum method and a fixed fluid mesh was capable of capturing realistic vascular flow and pressure behaviors. There were good predictions of flow and pressure waveforms down the length of a straight and a stenotic deformable phantom, indicating that the numerical simulation captured both the vessel wall motions and wave reflections accurately. Due to the good comparisons in pressure and flow, the impedance comparisons were also favorable. The simulated and measured flow and pressure results were similar to those previously measured *in-vivo*. The numerical simulation was able to track velocity patterns very well in regions with simple flow. In regions containing more complex and diverging flow, a finer mesh resolution was required for the simulation to capture the velocity patterns faithfully. The results presented in this paper show promising potential for the numerical technique to make accurate predictions of vascular tissue motion, and blood flow and pressure under the influence of blood vessel compliance. This study provides the cornerstone for further deformable validation studies involving more complex geometries, and *in-vivo* validation studies that could ultimately support the use of CFD into clinical medicine.

References

1. Caro CG, Fitz-Gerald JM, Schroter RC. (1971) Atheroma and arterial wall shear. Observation, correlation and proposal of a shear dependent mass transfer mechanism for atherogenesis. Proc R Soc Lond B Biol Sci. 17746:109-159.
2. Glagov S, Zarins C, Giddens DP, Ku DN. (1988) Hemodynamics and atherosclerosis. Insights and perspectives gained from studies of human arteries. Arch Pathol Lab Med. 11210:1018-1031.
3. Ku DN, Giddens DP, Zarins CK, Glagov S. (1985) Pulsatile flow and atherosclerosis in the human carotid bifurcation. Positive correlation between plaque location and low oscillating shear stress. Arteriosclerosis. 53:293-302.
4. Malek AM, Alper SL, Izumo S. (1999) Hemodynamic shear stress and its role in atherosclerosis. JAMA. 28221:2035-2042.
5. Vollmar JF, Paes E, Pauschinger P, Henze E, Friesch A. (1989) Aortic aneurysms as late sequelae of above-knee amputation. Lancet. 28667:834-835.
6. Guyton JR, Hartley CJ. (1985) Flow restriction of one carotid artery in juvenile rats inhibits growth of arterial diameter. Am J Physiol. 2484 Pt 2:H540-546.
7. Langille BL, Bendeck MP, Keeley FW. (1989) Adaptations of carotid arteries of young and mature rabbits to reduced carotid blood flow. Am J Physiol. 2564 Pt 2:H931-939.
8. Masuda H, Zhuang YJ, Singh TM, et al. (1999) Adaptive remodeling of internal elastic lamina and endothelial lining during flow-induced arterial enlargement. Arterioscler Thromb Vasc Biol. 1910:2298-2307.
9. Sho E, Sho M, Singh TM, Xu C, Zarins CK, Masuda H. (2001) Blood flow decrease induces apoptosis of endothelial cells in previously dilated arteries resulting from chronic high blood flow. Arterioscler Thromb Vasc Biol. 217:1139-1145.
10. Wolinsky H, Glagov S. (1967) A lamellar unit of aortic medial structure and function in mammals. Circ Res. 201:99-111.
11. Zhuang YJ, Singh TM, Zarins CK, Masuda H. (1998) Sequential increases and decreases in blood flow stimulates progressive intimal thickening. Eur J Vasc Endovasc Surg. 164:301-310.
12. Tai N, Salacinski H, Edwards A, Hamilton G, Seifalian A. (2000) Compliance properties of conduits used in vascular reconstruction. British Journal of Surgery. 8711:1516-1524.
13. Draney M, Arko F, Alley M, et al. (2004) Quantification of vessel wall motion and cyclic strain using cine phase contrast MRI: in vivo validation in the porcine aorta. Magnetic Resonance in Medicine. 522:286-295.
14. Cheng C, Herfkens R, Taylor C. (2003) Abdominal aortic hemodynamic conditions in healthy subjects aged 50-70 at rest and during lower limb exercise: in vivo quantification using MRI. Atherosclerosis. 1682:323-331.

15. Taylor CA, Hughes TJ, Zarins CK. (1998) Finite element modeling of three-dimensional pulsatile flow in the abdominal aorta: relevance to atherosclerosis. Ann Biomed Eng. 266:975-987.

16. Figueroa CA, Vignon-Clementel IE, Jansen KE, Hughes TJR, Taylor CA. (2006) A coupled momentum method for modeling blood flow in three-dimensional deformable arteries. Computer Methods in Applied Mechanics and Engineering. 19541-43:5685-5706.

17. Jou LD, Quick CM, Young WL, et al. (2003) Computational approach to quantifying hemodynamic forces in giant cerebral aneurysms. AJNR Am J Neuroradiol. 249:1804-1810.

18. Wentzel JJ, Gijsen FJ, Schuurbiers JC, et al. (2005) Geometry guided data averaging enables the interpretation of shear stress related plaque development in human coronary arteries. J Biomech. 387:1551-1555.

19. Anderson J, Wood HG, Allaire PE, Olsen DB. (2000) Numerical analysis of blood flow in the clearance regions of a continuous flow artificial heart pump. Artif Organs. 246:492-500.

20. Benard N, Perrault R, Coisne D. (2004) Blood flow in stented coronary artery: numerical fluid dynamics analysis. Conf Proc IEEE Eng Med Biol Soc. 5:3800-3803.

21. Li Z, Kleinstreuer C. (2005) Blood flow and structure interactions in a stented abdominal aortic aneurysm model. Med Eng Phys. 275:369-382.

22. Migliavacca F, Balossino R, Pennati G, et al. (2006) Multiscale modelling in biofluidynamics: application to reconstructive paediatric cardiac surgery. J Biomech. 396:1010-1020.

23. Taylor CA, Draney MT, Ku JP, et al. (1999) Predictive medicine: computational techniques in therapeutic decision-making. Comput Aided Surg. 45:231-247.

24. Vignon-Clementel IE, Figueroa CA, Jansen KE, Taylor CA. (2006) Outflow boundary conditions for three-dimensional finite element modeling of blood flow and pressure in arteries. Computer Methods in Applied Mechanics and Engineering. 19529-32:3776-3796.

25. Blanco PJ, Feijoo RA, Urquiza SA. (2007) A unified variational approach for coupling 3D-1D models and its blood flow applications. Computer Methods in Applied Mechanics and Engineering. 19641-44:4391-4410.

26. Formaggia L, Gerbeau JF, Nobile F, Quarteroni A. (2002) Numerical treatment of defective boundary conditions for the Navier-Stokes equations. Siam Journal on Numerical Analysis. 401:376-401.

27. Formaggia L, Moura A, Nobile F. (2007) On the stability of the coupling of 3d and 1d fluid-structure interaction models for blood flow simulations. Esaim-Mathematical Modelling and Numerical Analysis-Modelisation Mathematique Et Analyse Numerique. 414:743-769.

28. Formaggia L, Veneziani A, Vergara C. (2008) A New Approach to Numerical Solution of Defective Boundary Value Problems in Incompressible Fluid Dynamics. Siam Journal on Numerical Analysis. 466:2769-2794.

29. Lagana K, Balossino R, Migliavacca F, et al. (2005) Multiscale modeling of the cardiovascular system: application to the study of pulmonary and coronary

perfusions in the univentricular circulation. Journal of Biomechanics. 385:1129-1141.

30. Migliavacca F, Balossino R, Pennati G, et al. (2006) Multiscale modelling in biofluidynamics: Application to reconstructive paediatric cardiac surgery. Journal of Biomechanics. 396:1010-1020.

31. Long Q, Xu XY, Bourne M, Griffith TM. (2000) Numerical study of blood flow in an anatomically realistic aorto-iliac bifurcation generated from MRI data. Magn Reson Med. 434:565-576.

32. Rayz VL, Boussel L, Acevedo-Bolton G, et al. (2008) Numerical simulations of flow in cerebral aneurysms: comparison of CFD results and in vivo MRI measurements. J Biomech Eng. 1305:051011.

33. Acevedo-Bolton G, Jou LD, Dispensa BP, et al. (2006) Estimating the hemodynamic impact of interventional treatments of aneurysms: numerical simulation with experimental validation: technical case report. Neurosurgery. 592:E429-430; author reply E429-430.

34. Bertolotti C, Deplano V, Fuseri J, Dupouy P. (2001) Numerical and experimental models of post-operative realistic flows in stenosed coronary bypasses. J Biomech. 348:1049-1064.

35. Botnar R, Rappitsch G, Scheidegger MB, Liepsch D, Perktold K, Boesiger P. (2000) Hemodynamics in the carotid artery bifurcation: a comparison between numerical simulations and in vitro MRI measurements. J Biomech. 332:137-144.

36. Hoi Y, Woodward SH, Kim M, Taulbee DB, Meng H. (2006) Validation of CFD simulations of cerebral aneurysms with implication of geometric variations. J Biomech Eng. 1286:844-851.

37. Ku JP, Elkins CJ, Taylor CA. (2005) Comparison of CFD and MRI flow and velocities in an in vitro large artery bypass graft model. Ann Biomed Eng. 333:257-269.

38. Ford MD, Nikolov HN, Milner JS, et al. (2008) PIV-measured versus CFD-predicted flow dynamics in anatomically realistic cerebral aneurysm models. J Biomech Eng. 1302:021015.

39. Marshall I, Zhao S, Papathanasopoulou P, Hoskins P, Xu Y. (2004) MRI and CFD studies of pulsatile flow in healthy and stenosed carotid bifurcation models. J Biomech. 375:679-687.

40. Papathanasopoulou P, Zhao S, Kohler U, et al. (2003) MRI measurement of time-resolved wall shear stress vectors in a carotid bifurcation model, and comparison with CFD predictions. J Magn Reson Imaging. 172:153-162.

41. Brunette J, Mongrain R, Laurier J, Galaz R, Tardif JC. (2008) 3D flow study in a mildly stenotic coronary artery phantom using a whole volume PIV method. Med Eng Phys. 309:1193-1200.

42. Frauenfelder T, Lotfey M, Boehm T, Wildermuth S. (2006) Computational fluid dynamics: hemodynamic changes in abdominal aortic aneurysm after stent-graft implantation. Cardiovasc Intervent Radiol. 294:613-623.

43. Pekkan K, de Zelicourt D, Ge L, et al. (2005) Physics-driven CFD modeling of complex anatomical cardiovascular flows-a TCPC case study. Ann Biomed Eng. 333:284-300.

44. Ryu K, Healy TM, Ensley AE, Sharma S, Lucas C, Yoganathan AP. (2001) Importance of accurate geometry in the study of the total cavopulmonary connection: computational simulations and in vitro experiments. Ann Biomed Eng. 2910:844-853.
45. Wang C, Pekkan K, de Zelicourt D, et al. (2007) Progress in the CFD modeling of flow instabilities in anatomical total cavopulmonary connections. Ann Biomed Eng. 3511:1840-1856.
46. Gijsen FJ, Allanic E, van de Vosse FN, Janssen JD. (1999) The influence of the non-Newtonian properties of blood on the flow in large arteries: unsteady flow in a 90 degrees curved tube. J Biomech. 327:705-713.
47. Gijsen FJ, van de Vosse FN, Janssen JD. (1999) The influence of the non-Newtonian properties of blood on the flow in large arteries: steady flow in a carotid bifurcation model. J Biomech. 326:601-608.
48. Papaharilaou Y, Doorly DJ, Sherwin SJ. (2001) Assessing the accuracy of two-dimensional phase-contrast MRI measurements of complex unsteady flows. J Magn Reson Imaging. 146:714-723.
49. Perktold K, Hofer M, Rappitsch G, Loew M, Kuban BD, Friedman MH. (1998) Validated computation of physiologic flow in a realistic coronary artery branch. J Biomech. 313:217-228.
50. Bushberg J, Seibert J, Leidholdt Jr E, Boone J, Goldschmidt Jr E. (2003) The essential physics of medical imaging. Medical Physics. 30:1936.
51. Nishimura D. (1996) Principles of magnetic resonance imaging. Department of Electrical Engineering: Stanford University.
52. Nayler G, Firmin D, Longmore D. (1986) Blood flow imaging by cine magnetic resonance. Journal of computer assisted tomography. 105:715.
53. Whiting C, Jansen K. (2001) A stabilized finite element method for the incompressible Navier-Stokes equations using a hierarchical basis. International Journal for Numerical Methods in Fluids. 351:93-116.
54. Taylor C, Hughes T, Zarins C. (1998) Finite element modeling of blood flow in arteries. Computer Methods in Applied Mechanics and Engineering. 1581-2:155-196.
55. Gresho P, Sani R. (1998) Incompressible Flow and the Finite Element Method. Volume 2: Incompressible Flow and Finite Element: John Wiley and sons.
56. Hughes T, Hughes. (2000) The finite element method: linear static and dynamic finite element analysis: Dover Publications New York.
57. Grant BJ, Paradowski LJ. (1987) Characterization of pulmonary arterial input impedance with lumped parameter models. Am J Physiol. 2523 Pt 2:H585-593.
58. Krenz GS, Linehan JH, Dawson CA. (1992) A fractal continuum model of the pulmonary arterial tree. J Appl Physiol. 726:2225-2237.
59. Spilker RL, Feinstein JA, Parker DW, Reddy VM, Taylor CA. (2007) Morphometry-based impedance boundary conditions for patient-specific modeling of blood flow in pulmonary arteries. Ann Biomed Eng. 354:546-559.
60. Steele BN, Olufsen MS, Taylor CA. (2007) Fractal network model for simulating abdominal and lower extremity blood flow during resting and exercise conditions. Comput Methods Biomech Biomed Engin. 101:39-51.

61. Segers P, Brimioulle S, Stergiopulos N, et al. (1999) Pulmonary arterial compliance in dogs and pigs: the three-element windkessel model revisited. Am J Physiol. 2772 Pt 2:H725-731.
62. Stergiopulos N, Westerhof BE, Westerhof N. (1999) Total arterial inertance as the fourth element of the windkessel model. Am J Physiol. 2761 Pt 2:H81-88.
63. Wang JJ, Flewitt JA, Shrive NG, Parker KH, Tyberg JV. (2006) Systemic venous circulation. Waves propagating on a windkessel: relation of arterial and venous windkessels to systemic vascular resistance. Am J Physiol Heart Circ Physiol. 2901:H154-162.
64. Westerhof N, Lankhaar JW, Westerhof BE. (2009) The arterial Windkessel. Med Biol Eng Comput. 472:131-141.
65. Lotz J, Meier C, Leppert A, Galanski M. (2002) Cardiovascular flow measurement with phase-contrast MR imaging: basic facts and implementation. Radiographics. 223:651-671.
66. Bax L, Bakker CJ, Klein WM, Blanken N, Beutler JJ, Mali WP. (2005) Renal blood flow measurements with use of phase-contrast magnetic resonance imaging: normal values and reproducibility. J Vasc Interv Radiol. 166:807-814.
67. Greene ER, Venters MD, Avasthi PS, Conn RL, Jahnke RW. (1981) Noninvasive characterization of renal artery blood flow. Kidney Int. 204:523-529.
68. Les AS, Shadden SC, Figueroa CA, et al. Quantification of hemodynamics in abdominal aortic aneurysms during rest and exercise using magnetic resonance imaging and computational fluid dynamics. Ann Biomed Eng. 384:1288-1313.
69. Westerhof N, Elzinga G, Sipkema P. (1971) An artificial arterial system for pumping hearts. J Appl Physiol. 315:776-781.
70. Specht E. (2010) Packomania. In: The best known packings of equal circles in the unit circle. University of Magdeburg, Germany http://www.packomania.com/cci Accessed 5 May 2010.
71. Khunatorn Y, Shandas R, DeGroff C, Mahalingam S. (2003) Comparison of in vitro velocity measurements in a scaled total cavopulmonary connection with computational predictions. Ann Biomed Eng. 317:810-822.
72. Taylor C, Steinman D. Image-Based Modeling of Blood Flow and Vessel Wall Dynamics: Applications, Methods and Future Directions: Sixth International Bio-Fluid Mechanics Symposium and Workshop, March 28-30, 2008 Pasadena, California (Position Paper). Annals of Biomedical Engineering. 383:1188-1203.
73. Lagana K, Balossino R, Migliavacca F, et al. (2005) Multiscale modeling of the cardiovascular system: application to the study of pulmonary and coronary perfusions in the univentricular circulation. J Biomech. 385:1129-1141.
74. Tang BT, Cheng CP, Draney MT, et al. (2006) Abdominal aortic hemodynamics in young healthy adults at rest and during lower limb exercise: quantification using image-based computer modeling. Am J Physiol Heart Circ Physiol. 2912:H668-676.
75. Cebral JR, Lohner R. (2005) Efficient simulation of blood flow past complex endovascular devices using an adaptive embedding technique. IEEE Trans Med Imaging. 244:468-476.

76. Salsac A, Sparks S, Lasheras J. (2004) Hemodynamic changes occurring during the progressive enlargement of abdominal aortic aneurysms. Annals of vascular surgery. 181:14-21.

77. Olufsen MS. (2000) A one-dimensional fluid dynamic model of the systemic arteries. Stud Health Technol Inform. 71:79-97.

78. Elkins CJ, Markl M, Iyengar A, Wicker R, Eaton JK. (2004) Full-field velocity and temperature measurements using magnetic resonance imaging in turbulent complex internal flows. International Journal of Heat and Fluid Flow. 255:702-710.

79. Shankar P, Kumar M. (1994) Experimental determination of the kinematic viscosity of glycerol-water mixtures. Proceedings: Mathematical and Physical Sciences.573-581.

80. H.J. Kim CAF, T.J.R. Hughes, K.E. Jansen, C.A. Taylor. (2009) Augmented Lagrangian method for constraining the shape of velocity profiles at outlet boundaries for three-dimensional finite element simulations of blood flow. Comput Methods Appl Mech Engrg.

81. McCauley TR, Pena CS, Holland CK, Price TB, Gore JC. (1995) Validation of volume flow measurements with cine phase-contrast MR imaging for peripheral arterial waveforms. J Magn Reson Imaging. 56:663-668.

82. Kilner PJ, Firmin DN, Rees RS, et al. (1991) Valve and great vessel stenosis: assessment with MR jet velocity mapping. Radiology. 1781:229-235.

83. Oshinski J, Ku D, Pettigrew R. (1995) Turbulent fluctuation velocity: the most significant determinant of signal loss in stenotic vessels. Magnetic Resonance in Medicine. 332:193-199.

84. Taylor CA, Steinman DA. Image-based modeling of blood flow and vessel wall dynamics: applications, methods and future directions: Sixth International Bio-Fluid Mechanics Symposium and Workshop, March 28-30, 2008 Pasadena, California. 1188-1203 p.

85. Goergen C, Johnson B, Greve J, Taylor C, Zarins C. Increased anterior abdominal aortic wall motion: possible role in aneurysm pathogenesis and design of endovascular devices. Journal of Endovascular Therapy. 144:574-584.

86. Shipkowitz T, Rodgers V, Frazin L, Chandran K. (2000) Numerical study on the effect of secondary flow in the human aorta on local shear stresses in abdominal aortic branches. Journal of Biomechanics. 336:717-728.

87. Weydahl E, Moore J. (2001) Dynamic curvature strongly affects wall shear rates in a coronary artery bifurcation model. Journal of Biomechanics. 349:1189-1196.

88. Hager A, Kaemmerer H, Rapp-Bernhardt U, et al. (2002) Diameters of the thoracic aorta throughout life as measured with helical computed tomography. The Journal of Thoracic and Cardiovascular Surgery. 1236:1060.

89. Pearson A, Guo R, Orsinelli D, Binkley P, Pasierski T. (1994) Transesophageal echocardiographic assessment of the effects of age, gender, and hypertension on thoracic aortic wall size, thickness, and stiffness. American Heart Journal. 1282:344-351.

90. Dobrin P. (1978) Mechanical properties of arterises. Physiological reviews. 582:397.

91. O'Rourke M, Kelly R, Avolio A. (1992) The arterial pulse. Lea and Febiger.15-20.

92. Arcaute K, Wicker R. (2008) Patient-Specific Compliant Vessel Manufacturing Using Dip-Spin Coating of Rapid Prototyped Molds. Journal of Manufacturing Science and Engineering. 130:051008.

93. Cortez M, Quintana R, Wicker R. (2007) Multi-step dip-spin coating manufacturing system for silicone cardiovascular membrane fabrication with prescribed compliance. The International Journal of Advanced Manufacturing Technology. 347:667-679.

94. Mohiaddin R, Kilner P, Rees S, Longmore D. (1993) Magnetic resonance volume flow and jet velocity mapping in aortic coarctation. Journal of the American College of Cardiology. 225:1515.

95. Figueroa CA, Ku JP. (2010) SimVascular. https://simtk.org/home/simvascular Accessed 2010.

96. Love A. (1944) A Treatise on the Mathematical Theory of Elasticity. Dover Publications. New York.

97. H.J. Kim a CAFb, T.J.R. Hughes c, K.E. Jansen d, C.A. Taylor. (2009) Augmented Lagrangian method for constraining the shape of velocity profiles at outlet boundaries for three-dimensional finite element simulations of blood flow. Comput Methods Appl Mech Engrg.

98. Mills C, Gabe I, Gault J, et al. (1970) Pressure-flow relationships and vascular impedance in man. Cardiovasc Res. 44:405-417.

99. Remington J, Wood E. (1956) Formation of peripheral pulse contour in man. Journal of Applied Physiology. 93:433.

100. Stergiopulos N, Segers P, Westerhof N. (1999) Use of pulse pressure method for estimating total arterial compliance in vivo. American Journal of Physiology-Heart and Circulatory Physiology. 2762:H424.